Optical Materials 126 (2022) 112152

Contents lists available at ScienceDirect

Optical Materials

journal homepage: www.elsevier.com/locate/optmat

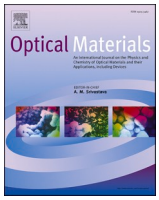

Valley topological line-defects for Terahertz waveguides and power divider

BoLin Li [a,b], HongYu Shi [a,b,*], Wei E.I. Sha [c], JianJia Yi [b], GuoQiang Li [a,b], AnXue Zhang [b], Zhuo Xu [a,d]

[a] MOE Key Laboratory for Multifunctional Materials and Structures, Xi'an Jiaotong University, Xi'an, 710049, China
[b] School of Electronic and Information Engineering, Xi'an Jiaotong University, Xi'an, 710049, China
[c] State Key Laboratory of Modern Optical Instrumentation, College of Information Science and Electronic Engineering, Zhejiang University, Hangzhou, China
[d] Electronic Materials Research Laboratory, Key Laboratory of the Ministry of Education, Xi'an Jiaotong University, Xi'an, 710049, China

ARTICLE INFO

Keywords:
Valley Hall photonic crystals
Line-defect edge states
Topological waveguides and power divider

ABSTRACT

Topological edge states exhibit low backscattering, unidirectional energy propagation, and robust immunity to sharp bends and defects in photonic topological waveguides. These properties of topological waveguides are expected to be applied in terahertz (THz) technology and expand to functional devices. Here, we introduce a line-defect into valley Hall photonic crystals (VPCs) and discuss the influence of line-defect to edge states of valley Hall photonic topological waveguide. The introduction of line-defect can greatly improve the design freedom of topological waveguides, and is expected to be extended to functional devices. We constructed a straight VPC waveguide and a Z-shaped VPC waveguide to verify the topological valley line-defect edge state and the single-mode transmission of topological line-defect states is excited by a rectangular waveguide with a tapered coupling structure. The VPC waveguide has low bending loss and a working bandwidth (return loss < -10 dB) from 0.4 to 0.422 THz. We propose a topological power divider (TPD) operating at THz frequencies and achieved -3.3 per port equal power divide. Furthermore, this TPD is robust against defects and is promising for on-chip THz integration.

1. Introduction

Photonic topological insulators (PTIs), which are "insulating" in the bulk but "conducting" at the edges [1–5]. PTIs have a robust edge-transmission ability with strongly suppressed backscattering caused by disorder and sharp bends without additional optimization. This type of robustness is called topological protection [1,2,5–8]. The edge state transmission with a topological protection in two dimensions can be realized by constructing topological waveguides [1–3,6–15] with spin-Hall PTIs [6–8,17] or valley Hall PTIs (also regarded as valley Hall photonic crystals(VPCs)) [1–3,8,9,11–15,18]. For spin-Hall PTIs, the structure with trivial-nontrivial PTIs [19] and trivial-nontrivial-trivial sandwich structure [16] are most common for topological edge states. Recently, different from the structure of trivial-nontrivial or trivial-nontrivial-trivial topologies, a topological waveguide has been realized in a structure of nontrivial PTIs-air-nontrivial PTIs in microwave band [6], which means that a line-defect is introduced. This topological edge state exhibits low backscattering, unidirectional energy propagation, and robust immunity to sharp bends and defects, similar to the topological edge states formed by trivial and nontrivial dielectric photonic crystals [17].

However, the topological waveguide designed on the basis of VPCs is limited to a domain wall between two VPCs with valley Chern number that is half-integer (1/2 or −1/2) with opposite signs [1–3]. Although VPCs waveguides have shown well transmission in previous work, the freedom of design method of topological waveguide is still limited. In addition, previous work on PTIs mostly focus on PTIs waveguides and observe the edge states of topological protection. PTIs have potential to design functional devices. There are works mentions the prototypes of beam splitters [7,15] and couplers [19] and observed the propagation behavior of spin-locking, but no devices performance is given and are difficult to connect with other types of waveguides that limits its application. The study of edge states of topological line defects will broaden the design methods of VPCs waveguides, and is expected to be applied in the design of topological functional devices (e.g., power dividers).

One of important application prospects of PTIs is for terahertz (THz) technology. THz spectral region [20–33] offers a wider available

* Corresponding author. MOE Key Laboratory for Multifunctional Materials and Structures, Xi'an Jiaotong University, Xi'an, 710049, China.
E-mail address: honyo.shi1987@gmail.com (H. Shi).

https://doi.org/10.1016/j.optmat.2022.112152
Received 23 December 2021; Received in revised form 20 February 2022; Accepted 23 February 2022

bandwidth than other frequency bands and combines the advantages of microwave communication with those of optical communication, such as high transmission rate, large capacity, strong directionality, and high security [32,33]. Thus, THz spectral band is key for the development of the next generation of communication [1], and thus compact and integrated THz devices are greatly desired. There is previous work on two-dimensional THz VPCs waveguide based on high-resistance silicon [1]. This THz topological waveguide achieved low-loss propagating through 10 sharp bends with zero radii and successful transmission of uncompressed 4K high-definition video in experiment. It can be seen that PTIs are one of the feasible solutions in THz communication, that has the advantage of insensitivity of defects such as fabrication imperfections, low bending loss at sharp corners and easy to integrate.

In this work, we introduce a line-defect into the VPCs and propose a topological power divider (TPD) for THz communication. On the one hand, we discussed the influence of the introduction of line-defect on the valley edge state and proposed straight and Z-shaped VPC waveguides using topological line-defect. The results verified that the valley topological line-defect edge state can be excited by connecting with a rectangular waveguide through a tapered coupler and the two VPCs waveguides exhibit good transmission and low reflection. On the other hand, we proposed a TPD and the TPD is composed of three VPCs waveguides. It is found that the proposed TPD can divide the transmission power equally, and no clear backscattering loss or modal change of transmission even after two sharp bends. Disorder is introduced into the TPD, which breaks the mirror symmetry of the TPD and no decrease in transmission performance is observed. In addition, proposed TPD makes up for the lack of application of PTIs in devices and paves the way for engineering applications of topological devices. High-performance topological devices are one of solutions for compact and miniaturization of THz systems, furthermore, the silicon-platform-based TPD has slight application prospects in the realization of the on-chip integrated system to realize the low propagation loss and low cost interconnection of components in the microsystem or microsystem-to-microsystem.

2. Design of the THz VPCs

The THz VPCs are all-Si circle columns with a height (h) of 190 μm and sandwiched between the plates of a parallel waveguide, as shown in Fig. 1(a). Each unit cell of the VPCs consists of two circle columns with an inner radius (r) of 25 μm and an outer radius R_1 or R_2. These unit cells have a diamond shape with an angle of 60° and a lattice constant (a) of 240μm. The distance between every two circle columns is $l = \sqrt{3}/3a$, which is also the side length of the Wigner–Seitz cell. Only the transverse-magnetic modes are considered, where magnetic fields are within the x–y plane. In the presence of inversion symmetry ($R_1 = R_2 = 2r = 50\mu m$), the VPC possesses a hexagonal C_6 symmetry that leads to a pair of degenerate Dirac points at the K and K' valleys in the band diagram at 0.38 THz (the green dotted line in Fig. 2(a)). After breaking the C_6 symmetry and reducing to the C_3 symmetry ($\Delta R = R_1 - R_2 \neq 0$), as shown in Fig. 1(d), the Dirac points disappear, opening a bandgap with a width depending on the ΔR between the first and second bands. For $\Delta R = 0.4r$ ($R_1 = 2r$ and $R_2 = 1.6r$), the bandgap is in the range from 0.39 to 0.444 THz (the red line in Fig. 2(a)). Fig. 2(b) shows VPC mode at the K and K′ valleys of first and second bands in the Wigner–Seitz. And the Berry curvatures which calculated using the first-principles method [1] are shown on the bottom right of Fig. 2(b). It can be clearly seen that four modes merge at the K and K' valleys in the first and second bands. Furthermore, the charities of the eigenmodes are reversed with respect to those at the K and K' valleys or to those at the first and second bands. Berry curvatures of VPCs localized and has opposite sign at K and K' valleys in the same band. From the Berry curvatures around different valleys, we get the half-integer Valley Chen numbers that $C_K = -1/2$ and $C_{K'} = 1/2$ at first band and $C_K = 1/2$ and $C_{K'} = -1/2$ at second band. These results are consistent with previous reports and can be verified numerically [1,12,13,17,20,35].

3. Topological valley transport with a line-defect

In previous works, the topological valley edge state was constructed via an interface between two VPCs with valley Chern numbers that is half-integer (1/2 or −1/2) with opposite signs. We introduce a line-defect in valley Hall PTIs (VPCs-air-VPCs structure), and the supercell of the proposed VPCs waveguide structure is shown in Fig. 3(a). The line-defect is placed at a domain wall between two VPCs that have

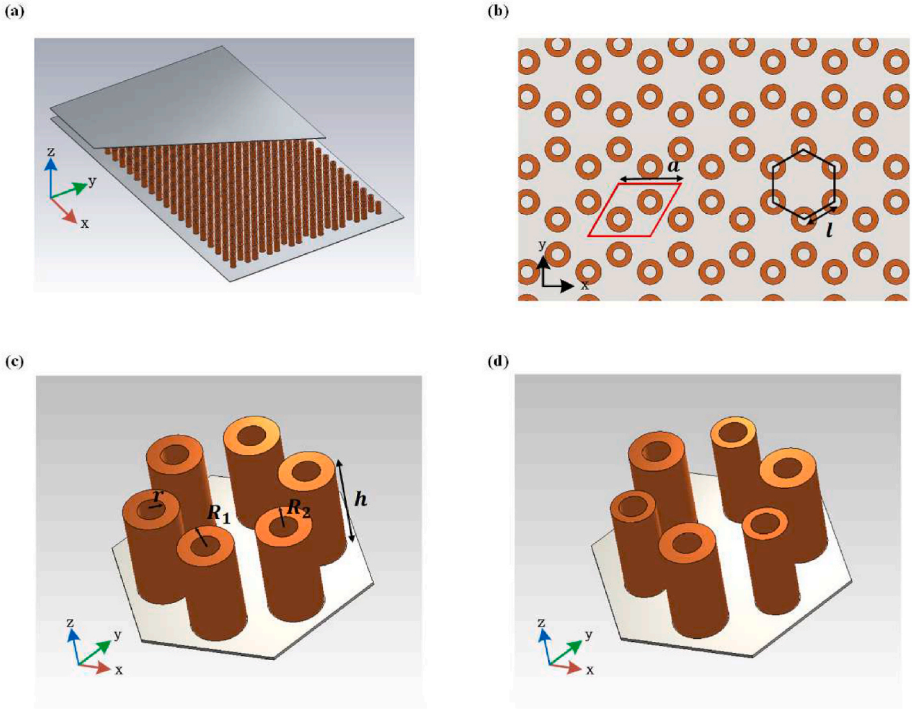

Fig. 1. Geometry of the VPCs. (a) The VPCs are sandwiched between the plates of a parallel waveguide. The materials of circle columns is high-resistivity (>10 k Ω cm) silicon with relative permittivity ε = 11.7. (b) Top view of the VPCs with the upper metal plate hidden. The red diamond shows the unit cell of the VPC, while the black hexagon shows the Wigner–Seitz cell. (c) A VPC with C6 symmetry. (d) A VPC with C6 symmetry breaking and C3 symmetry conservation. (For interpretation of the references to color in this figure legend, the reader is referred to the Web version of this article.)

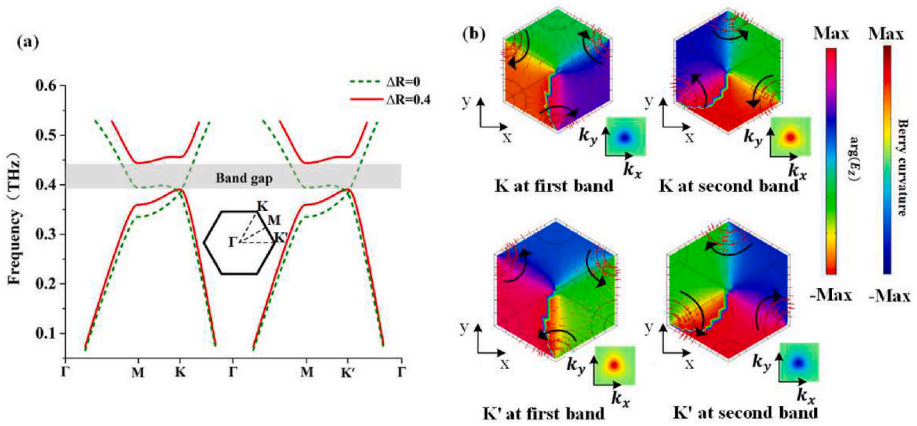

Fig. 2. Band structure of the THz VPC. (a) Band diagrams of the VPC. The green dotted line shows the VPC with C6 symmetry. The red line shows the VPC breaking the C6 symmetry and reducing to the C3 symmetry. (b) VPC mode at the K and K′ valleys for the first and second bands and Berry curvature near K or K′ points on the bottom right. The color description shows the phase of E_Z. The red arrows represent the Poynting vector, while the black arrow indicate the flow direction of the Poynting vector. The plotted range of Normalized Berry curvatures are around K or K′ valleys and centered at the K and K′ valleys. (For interpretation of the references to color in this figure legend, the reader is referred to the Web version of this article.)

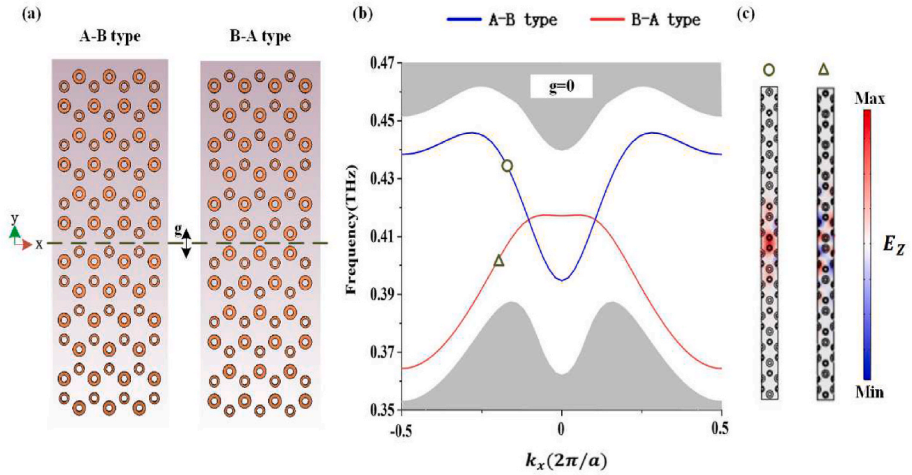

Fig. 3. Combination of VPCs with a line-defect. (a) Supercell of the proposed A-B type and B-A type VPCs waveguides. The width of the line-defect is g. (b) Band structure of the supercell with no line-defect. The blue and red line indicates the edge states, while the shaded regions mark the bulk bands. (c) Distribution of the electric field at the triangle and circle in (b). (For interpretation of the references to color in this figure legend, the reader is referred to the Web version of this article.)

opposite ΔR (which means they has Chern numbers with opposite signs.) and also a mirror symmetry about the y = 0 plane. The width of the introduced line defect is g. The proposed VPCs waveguide structure is different from nontrivial PTIs-air-nontrivial PTIs structure in Ref. [6]. In Ref. [6], the two nontrivial PTIs on either side of line-defect are two identical PTIs which are forming a nontrivial PTIs-air-nontrivial PTIs structure. However, the proposed VPCs waveguide directly introduces a line-defect in a domain wall between two VPCs that has half-integer Chern numbers with opposite signs which means the two VPCs beside the line-defect are two different VPCs.

We discussed the influence of different g widths on the edge states of VPCs-air-VPCs structure by sweeping k_x from $-\pi/a$ to π/a of the supercell of the waveguide structure. As shown in Fig. 3 (b). When g = 0, both A-B type and B-A type show one edge state in the band structure of the supercell of VPCs waveguide and they have opposite group velocities at K and K' valleys which is valley-momentum locking that is consistent with bulk-boundary correspondence. In Fig. 4, the introduction of line defects will affect the expression of valley edge states. As the width of g increase, the velocities at K and K' valleys of blue band are flattening out and the flanks become steep. At an appropriate line defect width such as $g = l/2$ and $g = 2l$, the Poynting vector of the blue band has pseudo-spin propagation which flow from one VPC to the next VPC with chirality structure, and electric field distributed around the line defect. It is similar to topological edge states. The frequency of red band keeps descend with g increase. When $g = 2l$, it almost close to the grey area, and electric field diverges in the VPCs. While g has a wider width such as $g = l$, as shown in Fig. 4(b), a new band appears in band structure of A-air-B type (the blue dashed line) and B-air-A type (the red dashed line) respectively. The red dashed band is in contact with the upper grey region and Poynting vector propagating in a straight line. Therefore, the red dashed band is no a topological edge state. The blue dashed band is within the bandgap and not in contact with the grey regions, but Poynting vector forms a complete spin which only flows in each supercell. It is no longer a useable guided-wave mode which similar to edge states of nontrivial PTIs-air-nontrivial PTIs structure in Ref. [6]. The two new bands also change with the line defect width. all the results are consistent with bulk-boundary correspondence. Comparing the six VPCs waveguides with line-defects of different widths, the A-air-B topological waveguide with a line defect width of $2l$ has the best performance, it has a wider bandwidth and the energy is concentrated in the line defects during propagation.

To further understand the topological valley line-defect edge state, we constructed a straight VPC waveguide (Fig. 5(a)) and a Z-shaped VPC waveguide (Fig. 5(b)) with two 60°bends, both with a zero radius of curvature. We designed a coupler with a length (m) of 9a and a width (w) of $2l$ (Fig. 5(c) and (d)) [1,36] to realize a smooth transition between the conventional hollow waveguide and the VPC waveguide.

The simulations were performed in the time domain solver of the CST Microwave Studio in a frequency range from 0.37 to 0.45 THz. As shown in Fig. 6(a), the reflection of straight and Z-shaped VPC waveguides is

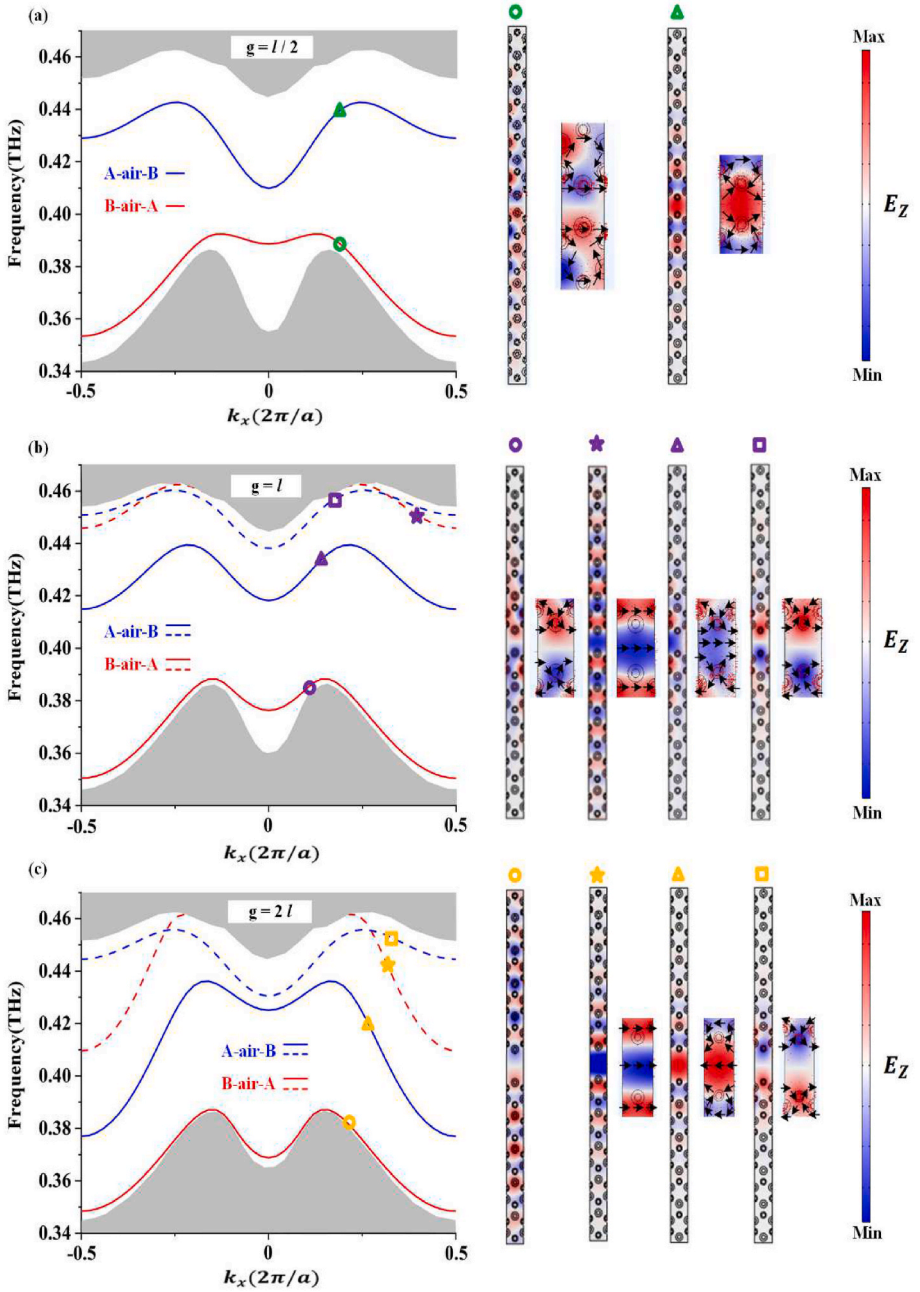

Fig. 4. Combination of VPC with a line-defect with different values of g. (a)–(c) Band structures of the supercells with g $= l/2$, g $= l$ and g $= 2l$. Distribution of the electric field and Poynting vector (the black arrows) at the circle, pentacle, triangle and rectangle in band structures are showing in the right.

weak in the linear range (the frequency in the grey area) of the band gap and reflection loss of Z-shaped VPC waveguide is slightly higher than straight. The VPC waveguide has a working bandwidth (<-10 dB) from 0.4 to 0.422 THz. The transmission simulation results are shown in Fig. 6 (b); these results indicate that the Z-shaped VPC waveguide does not introduce more back reflection compared with the straight VPC waveguide. Moreover, the two VPC waveguides exhibit a comparable bandwidth. The two 60°bends in the Z-shaped VPC waveguide induce a bending loss of about 0.14 dB minimum (approximately 0.07 dB per bend). The electric field distributions are shown in Fig. 6(c) and (d). In the Z-shaped VPC waveguide, the electric field goes through the continuous sharp turns smoothly, thus confirming the immunity to sharp bends. Additionally, the mode profile during transmission does not change after two 60°bends. The electric field of the tapered coupler is shown in Fig. 6(e). The electric field can smoothly transit from the rectangular waveguide to the topological waveguide without undergoing noticeable reflection or dissipation. These results correspond to the band structure of the supercell of VPCs waveguides. The topological valley line-defect edge state is excited by the tapered coupling structure, can achieve low-loss sharp bends transmission. Obvious reflections are observed near 0.43 THz corresponding to the blue band in Fig. 4 (a).

4. Design of the TPD

Using the designed VPCs waveguide, we propose an arrow-shaped TPD structure. As shown in Fig. 7(a), the TPS is composed of three straight VPC waveguides and exhibits a mirror symmetry. Unlike a regular power divider, the top (down) VPC waveguide is connected with a 60°sharp bend to the VPC waveguide parallel to the *x*-axis. Due to the line-defect introduced in the VPCs waveguide and the structural

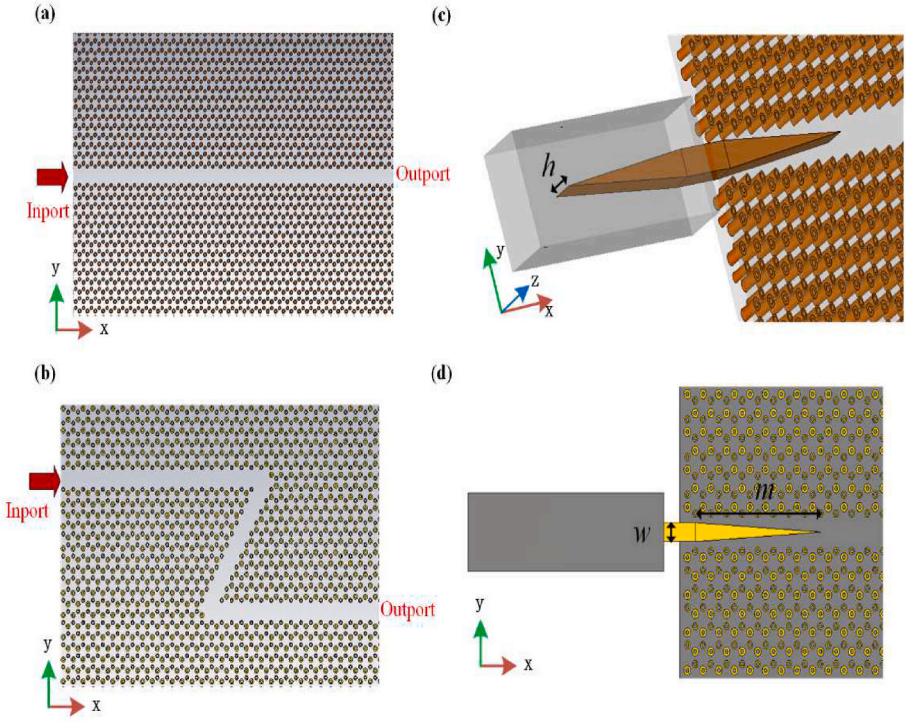

Fig. 5. VPC waveguide and tapered coupling structure. (a) Straight VPC waveguide. (b) Z-shaped VPC waveguide with two 60°bends, both with a radius of curvature of zero. (c) Overall view of the tapered coupling structure. (d) Top view of the tapered coupling structure connecting the rectangular waveguide with the VPC waveguide.

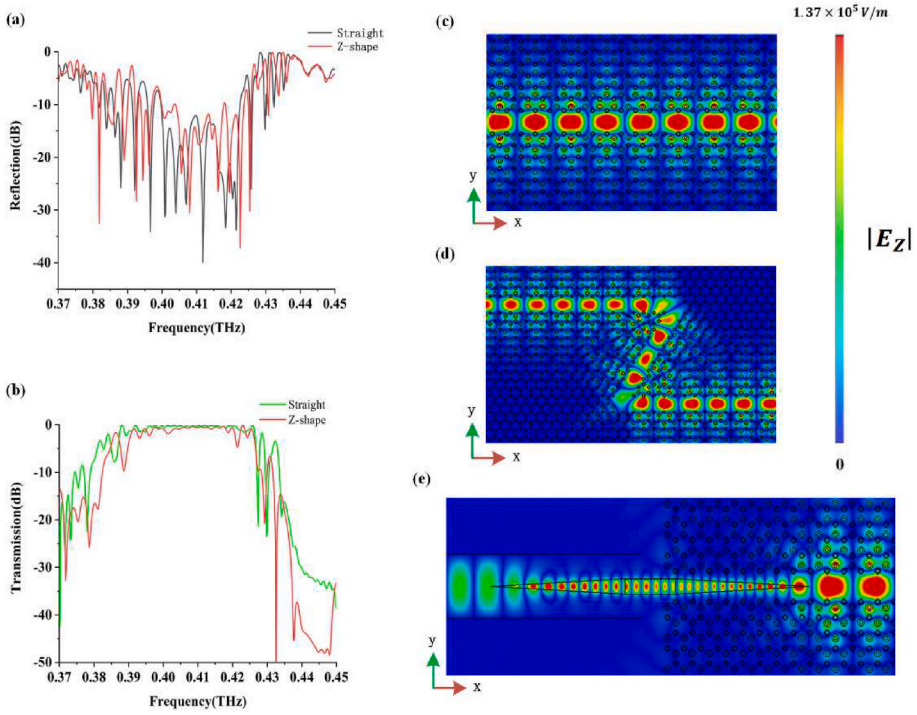

Fig. 6. Simulation results of the VPC waveguides. (a) Reflection of the straight and Z-shaped VPC waveguides. (b) Transmission of the straight VPC waveguide (the green line) and the Z-shaped VPC waveguide (the red line). (c) Electric field distribution of the straight VPC waveguide. (d) Electric field distribution of the Z-shaped VPC waveguide. (e) Electric field distribution of the tapered coupler interconnecting the rectangular waveguide with the VPC waveguide. (For interpretation of the references to color in this figure legend, the reader is referred to the Web version of this article.)

characteristics of VPCs, there will be extra VPCs waveguide, which is B-air-A type and the value of *g* is *l*. The band structure of the supercell of this VPCs waveguide are showing in Fig. 4(b). Because of the introduction of a narrow line-defect, no new band (the purple band) is generated and the frequency of edge state band (the green band) is almost move out of the band gap that exhibits a stop band in the 0.39–0.445 THz frequency band for reducing the undesired direct transmission. All-silicon dielectric waveguides with 30° radian are set up at 2-port and 3-port to facilitate port settings in the simulation.

The simulation results for the reflection and transmission of the proposed TPD are shown in Fig. 7(b). The reflection curve shows a working bandwidth close to the straight VPC waveguide, and the mirror-

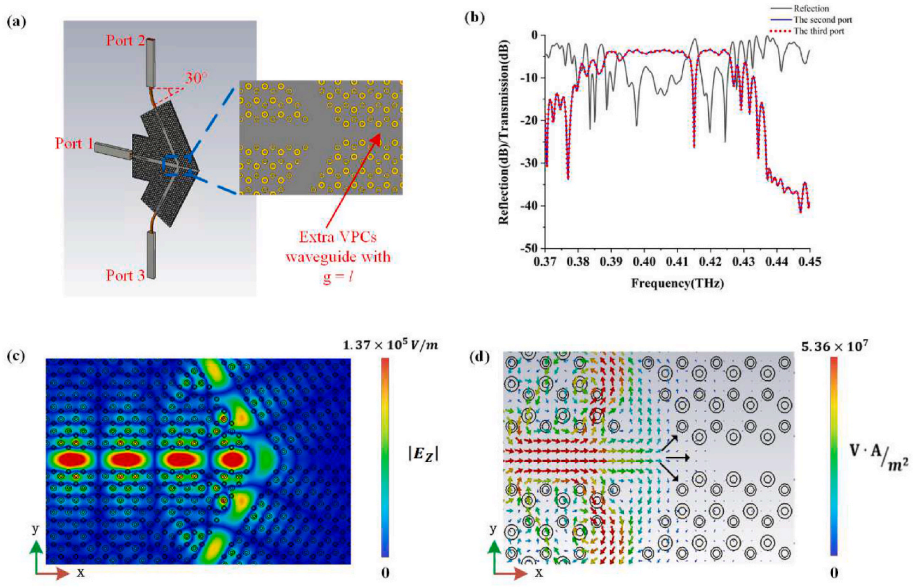

Fig. 7. Schematic of the proposed TPD and corresponding simulation results. (a) Entire structure of the TPD and rightmost of the arrow shape. (b) Reflection (the black line) and transmission curves of the second (the blue line) and third (the red dotted line) ports of the TPD. (c) Electric field distribution of the TPD. (d) Poynting vector of the TPD. The black arrow indicates the flow direction of the Poynting vector. (For interpretation of the references to color in this figure legend, the reader is referred to the Web version of this article.)

symmetry structure renders the transmission curves of the second and third ports identical; thus a transmittance of −3.3 dB per port can be reached. From Fig. 7(c), it can be seen that the energy flux of the electric field is equally divided at the arrow location and flows smoothly into the top and bottom VPC waveguides, respectively. No energy is observed to flow out of the VPCs waveguide on the right, which corresponds to the discussion of band structure of the supercell of VPCs waveguide. The proposed TPD can also be connected to the Z-waveguide to flexibly change the direction of the output or input ports to facilitate a connection with other systems. However, a reflection that can reach −7.5 dB is located near 0.4 THz, and an almost total reflection is located 0.415 THz within the working bandwidth. Fig. 7(d) shows the Poynting vector of the TPD at the rightmost of the arrow shape, where a part of the energy is divided equally at the end of the input waveguide and flows into the two output waveguides, while the other part of the energy continues to flow toward the top of the arrow, causing a reflection.

In order to reduce these reflections, a minor period adjustment was made to the structure of the TPD (as shown in Fig. 8. (a)). The reflection and transmission simulation results of the improved TPD are shown in Fig. 8(b). It can be seen that the reflections at 0.4 and 0.415 THz have been significantly improved. Fig. 8(c) and (d) show the corresponding electric field and Poynting vector of the improved TPD. The small back reflection near 0.39 THz is due to the mode and impedance mismatching between the tapered coupler and the TPD.

Traditional equal power dividers require a complete mirror-symmetric structure to maintain stable performance. Once the mirror-symmetric structure is broken, as can occur through manufacturing deviations or wear caused during use, their performance will deteriorate sharply. In order to prove the robustness of the proposed TPD, we removed a circle column close to the line-defect of the TPD (see the right-hand side of Fig. 9(a)), which results in a broken mirror-symmetry. The results are shown in Fig. 9(b). The reflection curve exhibits no clear change, while a considerable change can be observed in the transmission curves of the second and third ports. It can be seen that the blue and red dotted lines are no longer completely consistent, but the transmission performance is not reduced compared with that shown in Fig. 8(b) and

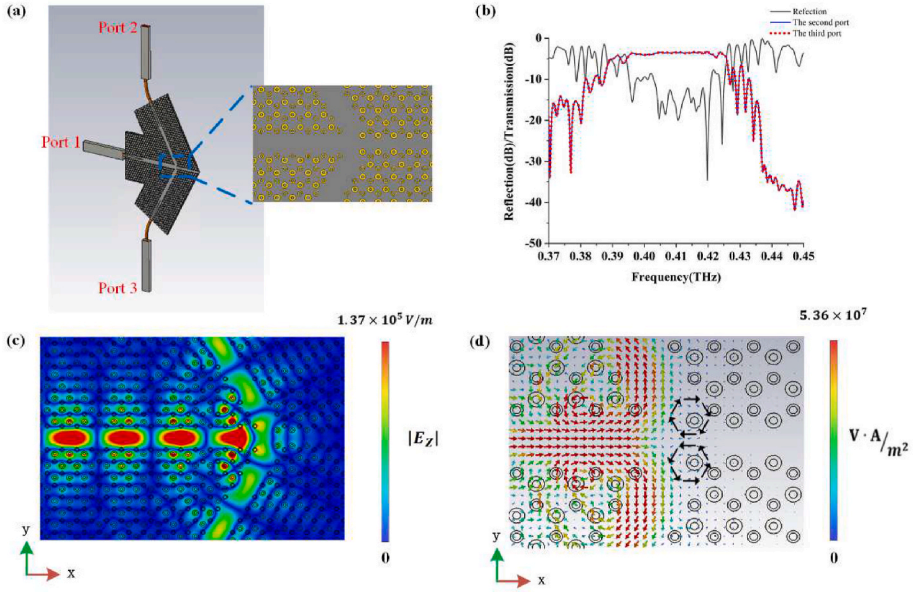

Fig. 8. Schematic of the improved TPD and corresponding simulation results. (a) Entire structure of the improved TPD and rightmost of the arrow shape. (b) Reflection (the black line) and transmission curves of the second (the blue line) and third (the red dotted line) ports of the improved TPD. (c) Electric field distribution of the improved TPD. (d) Poynting vector of the improved TPD. The black arrow indicates the flow direction of the Poynting vector. (For interpretation of the references to color in this figure legend, the reader is referred to the Web version of this article.)

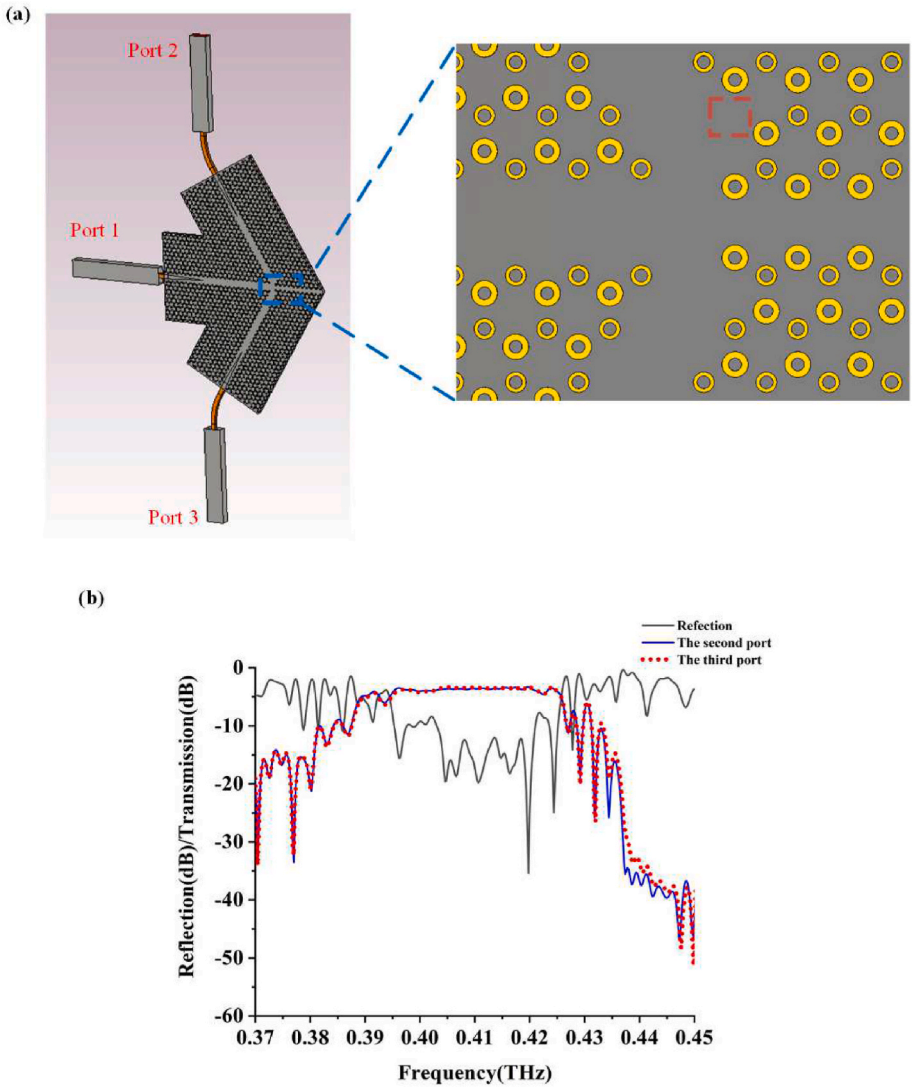

Fig. 9. Schematic of the TPD with disorder and corresponding simulation results. (a) Structure of the TPD with disorder and schematic of the disorder on the right-hand side of the image. (b) Reflection and transmission curves of the TPD with disorder.

this robust performance becomes more prominent when the output waveguide is longer. Therefore, the proposed TPD has robust performance that is beneficial for coping with manufacturing deviations.

5. Conclusion

In summary, a TPD working in THz range is proposed by introducing a line-defect into the VPCs. The results show that the proposed TPD can achieve equal power distribution and has a certain working bandwidth which correspond to the discussion of the supercell of VPCs waveguide that compose TPD. The robustness of the proposed TPD was confirmed even in the case of broken mirror symmetry: the TPD could still achieve equal power distribution, and no deterioration was observed. The robustness of the proposed TPD will be helpful for integrated THz systems with dimensions of only a few centimeters for future on-chip communication. On the one hand, the proposed TPD is robust against manufacturing deviations, and, on the other hand, it expands the application of PTI from waveguides to functional topological devices that fills the vacancy of PTI research in device applications and is expected to be applied to the on-chip integration to the interconnection of microsystems. Furthermore, THz topological devices is also one of the solutions to realize the compact, miniaturization and high-speed communication of THz systems. Although topological devices are far from traditional devices in practical applications, they have huge application potential.

CRediT authorship contribution statement

BoLin Li: Methodology, Writing – original draft, Validation, Visualization, Data curation. **HongYu Shi:** Methodology, Writing – original draft, Funding acquisition. **Wei E.I. Sha:** Writing – review & editing. **JianJia Yi:** Writing – review & editing. **GuoQiang Li:** Visualization, Data curation. **AnXue Zhang:** Writing – review & editing, Formal analysis. **Zhuo Xu:** Formal analysis, All authors have read and agreed to the published version of the manuscript.

Declaration of competing interest

The authors declare that they have no known competing financial interests or personal relationships that could have appeared to influence the work reported in this paper.

References

[1] Y.H. Yang, Y. Yamagami, X.B. Yu, P. Pitchappa, J. Webber, B.L. Zhang, M. Fujita, T. Nagatsuma, R. Singh, Terahertz topological photonics for on-chip communication, Nat. Photonics 14 (7) (2020) 446.

[2] S. Barik, H. Miyake, W. Degottardi, E. Waks, M. Hafezi, Two-dimensionally confined topological edge states in photonic crystals, New J. Phys. 18 (2016) 113013.

[3] F. Gao, H. Xue, Z. Yang, K. Lai, Y. Yu, X. Lin, Y. Chong, G. Shvets, B. Zhang, Topologically protected refraction of robust kink states in valley photonic crystals, Nat. Phys. 14 (2) (2018) 140.

[4] L. Lu, J.D. Joannopoulos, M. Soljačić, Topological photonics, Nat. Photonics 8 (11) (2014) 821–829.

[5] F.D.M. Haldane, S. Raghu, Possible realization of directional optical waveguides in photonic crystals with broken time-reversal symmetry, Phys. Rev. Lett. 100 (1) (2008), 013904.

[6] M.L.N. Chen, L.J. Jiang, Z.H. Lan, W.E.I. Sha, Pseudospin-Polarized topological line defects in dielectric photonic crystals, IEEE Trans. Antenn. Propag. 68 (1) (2020) 609.

[7] Q.L. Chen, L. Zhang, S. Xu, Z.J. Wang, E.P. Li, Y.H. Yang, H.S. Chen, Robust waveguiding in substrate-integrated topological photonic crystals, Appl. Phys. Lett. 116 (23) (2020) 231106.

[8] M.L.N. Chen, L.J. Jiang, Z.H. Lan, W.E.I. Sha, Coexistence of pseudospin-and valley-Hall-like edge states in a photonic crystal with C3v symmetry, Phys. Rev. Research 2 (4) (2020), 043148.

[9] J.W. Dong, X.D. Chen, H. Zhu, Y. Wang, X. Zhang, Valley photonic crystals for control of spin and topology, Nat. Mater. 16 (3) (2017) 298.

[10] M.I. Shalaev, W. Walasik, A. Tsukernik, Y. Xu, N.M. Litchinitser, Robust topologically protected transport in photonic crystals at telecommunication wavelengths, Nat. Nanotechnol. 14 (1) (2019) 98.

[11] X.T. He, E.T. Liang, J.J. Yuan, H.Y. Qiu, J.W. Dong, A silicon-on-insulator slab for topological valley transport, Nat. Commun. 10 (2019) 872.

[12] X.D. Chen, F.L. Zhao, M. Chen, J.W. Dong, Valley-contrasting physics in all-dielectric photonic crystals: orbital angular momentum and topological propagation, Phys. Rev. B 96 (2) (2017), 020202.

[13] T. Ma, G. Shvets, All-Si valley-Hall photonic topological insulator, New J. Phys. 18 (2016), 025012.

[14] J. Noh, H. Sheng, K.P. Chen, M.C. Rechtsman, Observation of photonic topological valley-Hall edge states, Phys. Rev. Lett. 120 (6) (2017), 063902.

[15] X. Wu, M. Yan, J. Tian, Y. Huang, W. Wen, Direct observation of valley-polarized topological edge states in designer surface plasmon crystals, Nat. Commun. 8 (2017) 1304.

[16] Y.F. Gao, Z. Jiang, L.L. Zhang, L. He, J. Zhao, Unidirectional propagation of coupled edge states in sandwich topological photonic crystals, J. Appl. Phys. 124 (21) (2018) 213107.

[17] L.H. Wu, H. Xiao, Scheme for achieving a topological photonic crystal by using dielectric material, Phys. Rev. Lett. 114 (22) (2015) 223901.

[18] Q. Chen, L. Zhang, M.J. He, Z.J. Wang, X. Lin, F. Gao, Y.H. Yang, B.L. Zhang, H. Chen, Valley-Hall photonic topological insulators with dual-band kink states, Adv. Opt. Mater. 7 (15) (2019) 1900036.

[19] R.J. Davis, D.J. Bisharat, D.F. Sievenpiper, Classical-to-topological transmission line couplers, Appl. Phys. Lett. 118 (13) (2021) 131102.

[20] M.Y. Frankel, S. Gupta, J.A. Valdmanis, G.A. Mourou, Terahertz attenuation and dispersion characteristics of coplanar transmission lines, IEEE Trans. Microw. Theor. Tech. 39 (6) (1991) 910–916.

[21] P.H. Siegel, Terahertz technology in biology and medicine, IEEE Trans. Microw. Theor. Tech. 52 (10) (2004) 2438–2447.

[22] W. Kanglin, D.M. Mittleman, Metal wires for terahertz wave guiding, Nature 432 (7015) (2004) 376–379.

[23] Y. Liang, H. Yu, H.C. Zhang, C. Yang, T.J. Cui, On-chip sub-terahertz surface plasmon polariton transmission lines in CMOS, Sci. Rep. 5 (2015) 14853.

[24] M.Y. Frankel, S. Gupta, Terahertz attenuation and dispersion characteristics of coplanar transmission lines, IEEE Trans. Microw. Theor. Tech. 39 (6) (1991) 910–916.

[25] S. Atakaramians, S. Afshar V, T.M. Monro, D. Abbott, Terahertz dielectric waveguides, Adv. Opt Photon 5 (2) (2013) 169–215.

[26] K.L. Wang, D.M. Mittleman, Metal wires for terahertz wave guiding, Nature 432 (7015) (2004) 376–379.

[27] J.A. Harrington, R. George, P. Pedersen, E. Mueller, Hollow polycarbonate waveguides with inner Cu coatings for delivery of terahertz radiation, Opt Express 12 (21) (2004) 5263–5268.

[28] L.F. Ye, Y. Chen, G.X. Cai, N. Liu, J.F. Zhu, Z.Y. Song, Q.H. Liu, Broadband absorber with periodically sinusoidally-patterned graphene layer in terahertz range, Opt Express 25 (10) (2017) 11223–11232.

[29] X.Y. He, F. Liu, F.T. Lin, W.Z. Shi, Investigation of terahertz all-dielectric metamaterials, Opt Express 27 (10) (2019) 13831–13844.

[30] B. Yu, Y. Ye, X. Ding, Y. Liu, Z.W. Xu, X.G. Liu, Q.J. Gu, Ortho-mode sub-THz interconnect channel for planar chip-to-chip communications, IEEE Trans. Microw. Theor. Tech. 66 (4) (2018) 1864–1873.

[31] B. Ferguson, X.C. Zhang, Materials for terahertz science and technology, Nat. Mater. 1 (1) (2002) 26–33.

[32] T. Nagatusma, G. Ducournau, C.C. Renaud, Advances in terahertz communications accelerated by photonics, Nat. Photonics 10 (6) (2016) 371–379.

[33] J.J. Ma, R. Shrestha, J. Adelberg, C.Y. Yeh, Z. Hossain, E. Knightly, J.M. Jornet, D. M. Mittleman, Security and eavesdropping in terahertz wireless links, Nature 563 (7729) (2018) 89.

[35] S.A. Skirlo, L. Lu, M. Soljacic, Multimode one-way waveguides of large chern numbers, Phys. Rev. Lett. 113 (11) (2014) 113904.

[36] X.B. Yu, J.Y. Kim, M. Fujita, T. Nagatsuma, Efficient mode converter to deep-subwavelength region with photonic-crystal waveguide platform for terahertz applications, Opt Express 27 (20) (2019) 28707–28721.